We are IntechOpen, the world's leading publisher of Open Access books Built by scientists, for scientists

6,900
Open access books available

185,000
International authors and editors

200M
Downloads

Our authors are among the

154
Countries delivered to

TOP 1%
most cited scientists

12.2%
Contributors from top 500 universities



WEB OF SCIENCE™

Selection of our books indexed in the Book Citation Index in Web of Science™ Core Collection (BKCI)

Interested in publishing with us?
Contact book.department@intechopen.com

Numbers displayed above are based on latest data collected.
For more information visit www.intechopen.com



25

Surface-Emitting Circular Bragg Lasers – A Promising Next-Generation On-Chip Light Source for Optical Communications

Xiankai Sun and Amnon Yariv
Department of Applied Physics, California Institute of Technology, Pasadena, California 91125, USA

1. Introduction

Surface-emitting lasers have been attracting people's interest over the past two decades because of their salient features such as low-threshold current, single-mode operation, and wafer-scale integration (Iga, 2000). Their low-divergence surface-normal emission also facilitates output coupling and packaging. Although Vertical Cavity Surface Emitting Lasers (VCSELs) have already been commercially available, their single-modedness and good emission pattern are guaranteed only for devices with a small mode area (diameter of ~μm). Attempts of further increase in the emission aperture have failed mostly because of the contradictory requirements of large-area emitting aperture and single modedness, which casts a shadow over the usefulness of VCSELs in high-power applications.

A highly desirable semiconductor laser will consist of a large aperture (say, diameter larger than 20 μm) emitting vertically (i.e., perpendicularly to the plane of the laser). It should possess the high efficiency typical of current-pumped, edge-emitting semiconductor lasers and, crucially, be single-moded. Taking a clue from the traditional edge-emitting distributed feedback (DFB) semiconductor laser, we proposed employing transverse circular Bragg confinement mechanism to achieve the goals and those lasers are accordingly referred to as "circular Bragg lasers."

There have been intensive research activities in planar circular grating lasers since early 1990s. Erdogan and Hall were the first to analyze their modal behavior with a coupled-mode theory (Erdogan & Hall, 1990, 1992). Wu et al. were the first to experimentally realize such lasers in semiconductors (Wu et al., 1991; Wu et al., 1992). With a more rigorous theoretical framework, Shams-Zadeh-Amiri et al. analyzed their above-threshold properties and radiation fields (Shams-Zadeh-Amiri et al., 2000, 2003). More recently, organic polymers are also used as the gain medium for these lasers due to their low fabrication cost (Jebali et al., 2004; Turnbull et al., 2005; Chen et al., 2007).

The circular gratings in the above-referenced work are designed radially periodic. In 2003 we proposed using Hankel-phased, i.e., radially chirped, gratings to achieve optimal interaction with the optical fields (Scheuer & Yariv, 2003), since the eigenmodes of the wave equation in cylindrical coordinates are Hankel functions. With their grating designed to follow the phases of Hankel functions, these circular Bragg lasers usually take three

Source: Frontiers in Guided Wave Optics and Optoelectronics, Book edited by: Bishnu Pal,
ISBN 978-953-7619-82-4, pp. 674, February 2010, INTECH, Croatia, downloaded from SCIYO.COM

configurations as shown in Fig. 1: (a) circular DFB laser, in which the grating extends from the center to the exterior boundary x_b; (b) disk Bragg laser, in which a center disk is surrounded by a radial Bragg grating extending from x_0 to x_b; (c) ring Bragg laser, in which an annular defect is surrounded by both inner and outer gratings extending respectively from the center to x_L and from x_R to x_b. Including a second-order Fourier component, the gratings are able to provide in-plane feedback as well as couple laser emission out of the resonator plane in vertical direction.

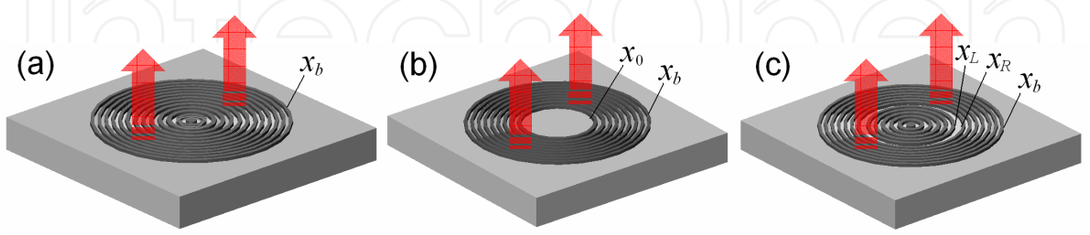


Fig. 1. Surface-emitting circular Bragg lasers: (a) circular DFB laser; (b) disk Bragg laser; (c) ring Bragg laser. Laser emission is coupled out of the resonator plane in vertical direction via the Bragg gratings

This chapter will present a comprehensive and systematic study on the surface-emitting Hankel-phased circular Bragg lasers. It is structured in the following manner: Sec. 2 focuses on every aspect in solving the modes of the lasers – analytical method, numerical method, and mode-solving accuracy check. Sec. 3 gives near-threshold modal properties of the lasers; comparison of different types of lasers demonstrates the advantages of disk and ring Bragg lasers in high-efficiency surface laser emission. Sec. 4 discusses above-threshold modal behavior, nonuniform pumping effect, and optimal design for different types of lasers. Sec. 5 concludes this chapter and suggests directions for future research.

2. Mode solving techniques

Taking into account the resonant vertical laser radiation, Appendix A presents a derivation of a comprehensive coupled-mode theory for the Hankel-phased circular grating structures in active media. The effect of vertical radiation is incorporated into the coupled in-plane wave equations by a numerical Green's function method. The in-plane (vertically confined) electric field is expressed as

$$E(x) = A(x)H_m^{(1)}(x) + B(x)H_m^{(2)}(x), \tag{1}$$

where $H_m^{(1)}(x)$ and $H_m^{(2)}(x)$ are the mth-order Hankel functions which represent respectively the in-plane outward and inward propagating cylindrical waves. A set of evolution equations for the amplitudes $A(x)$ and $B(x)$ is obtained:

$$\frac{\mathrm{d}A(x)}{\mathrm{d}x} = u(x)\cdot A(x) - v(x)\cdot B(x)\cdot e^{2i\delta\cdot x}, \tag{2}$$

$$\frac{\mathrm{d}B(x)}{\mathrm{d}x} = -u(x)\cdot B(x) + v(x)\cdot A(x)\cdot e^{-2i\delta\cdot x}, \tag{3}$$

where

$x = \beta\rho$: normalized radial coordinate with β being the in-plane propagation constant;
$\delta = (\beta_{design}-\beta)/\beta$: frequency detuning factor, representing a relative frequency shift of a resonant mode from the designed value;

$$u(x)=\begin{cases} g_A(x)-h_1, & \text{if } x \text{ is within a grating region} \\ g_A(x), & \text{if } x \text{ is within a no-grating region;} \end{cases}$$

$$v(x)=\begin{cases} h_1+ih_2, & \text{if } x \text{ is within a grating region} \\ 0, & \text{if } x \text{ is within a no-grating region;} \end{cases}$$

$h_1 = h_{1r} + ih_{1i}$: grating's radiation coupling coefficient, representing the effect of vertical laser radiation on the in-plane modes;
h_2: grating's feedback coupling coefficient, which can always be chosen real;
$g_A(x) = g(x) - \alpha$: space-dependent net gain coefficient, the minimum value of which required to achieve laser emission will be solved analytically or numerically;
α: nonsaturable internal loss, including absorption and nonradiative scattering losses;
$g(x) = g_0(x)/[1 + I(x)/I_{sat}]$: intensity-dependent saturated gain profile;
$g_0(x)$: unsaturated gain profile; and
$I(x)/I_{sat}$: field intensity distribution in units of saturation intensity.

It should be noted that, although Eqs. (2) and (3) appear to be a set of coupled equations for in-plane waves only, they implicitly include the effect of vertical radiation due to h_1. As it will become clearer in Sec. 2.3, the vertical radiation can simply be treated as a loss term during the process of solving the in-plane laser modes.

2.1 Analytical mode solving method

When solving the modes at threshold with uniform gain (or pump) distribution across the device, the net gain coefficient g_A is x independent. The generic solutions of Eqs. (2) and (3) in no-grating regions are trivial:

$$A(x) = A_0 e^{g_A x}, \tag{4}$$

$$B(x) = B_0 e^{-g_A x}. \tag{5}$$

In grating regions, by introducing $\tilde{A}(x) = A(x)e^{-i\delta x}$ and $\tilde{B}(x) = B(x)e^{i\delta x}$, Eqs. (2) and (3) become:

$$\frac{\mathrm{d}\tilde{A}(x)}{\mathrm{d}x} = (u - i\delta)\,\tilde{A}(x) - v\tilde{B}(x), \tag{6}$$

$$\frac{\mathrm{d}\tilde{B}(x)}{\mathrm{d}x} = -(u - i\delta)\,\tilde{B}(x) + v\tilde{A}(x), \tag{7}$$

whose generic solutions lead to

$$A(x) = A(0)e^{i\delta x}\,\frac{\sinh[S(x-L)] + \mathbb{C}\cosh[S(x-L)]}{-\sinh[SL] + \mathbb{C}\cosh[SL]}, \tag{8}$$

$$B(x)=\frac{A(0)e^{-i\delta x}}{v}\cdot\frac{[(u-i\delta)-\mathbb{C}S]\sinh[S(x-L)]+[\mathbb{C}(u-i\delta)-S]\cosh[S(x-L)]}{-\sinh[SL]+\mathbb{C}\cosh[SL]}, \tag{9}$$

where $S\equiv\sqrt{(u-i\delta)^2-v^2}$, $\mathbb{C}$ is a constant to be determined by specific boundary conditions, and L is a normalized length parameter (see Fig. 2). The determination of the constant $\mathbb{C}$ in Eqs. (8) and (9) requires the specific boundary conditions be applied to the grating under investigation.

We focus on two typical boundary conditions to obtain $\mathbb{C}$ and the corresponding field reflectivity in each case.

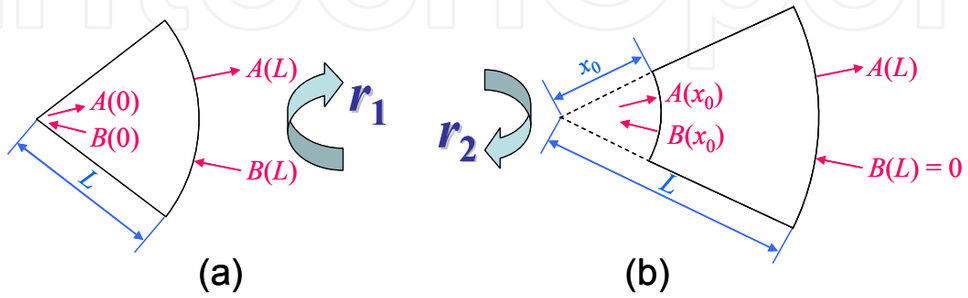


Fig. 2. Two types of boundary conditions for calculating reflectivities. (a) $A(0) = B(0)$, $r_1(L) = A(L)/B(L)$; (b) $B(L) = 0$, $r_2(x_0, L) = B(x_0)/A(x_0)$

Case I: As shown in Fig. 2(a), the grating extends from the center $x = 0$ to $x = L$. An inward propagating wave with amplitude $B(L)$ impinges from outside on the grating. The reflectivity is defined as $r_1(L) = A(L)/B(L)$. The finiteness of $E(x)$ at the center $x = 0$ requires $A(0) = B(0)$, leading to

$$\mathbb{C}=\frac{(u-v-i\delta)\sinh[SL]+S\cosh[SL]}{S\sinh[SL]+(u-v-i\delta)\cosh[SL]}$$

and to the reflectivity

$$r_1(L)=\frac{A(L)}{B(L)}=e^{2i\delta L}\frac{(u-v-i\delta)\sinh[SL]+S\cosh[SL]}{-(u-v-i\delta)\sinh[SL]+S\cosh[SL]}. \tag{10}$$

Case II: As shown in Fig. 2(b), the grating extends from $x = x_0$ to $x = L$. An outward propagating wave with amplitude $A(x_0)$ impinges from inside on the grating. The reflectivity is defined as $r_2(x_0, L) = B(x_0)/A(x_0)$. No inward propagating wave comes from outside of the grating, i.e., $B(L) = 0$. This condition leads to $\mathbb{C}=S/(u-i\delta)$ and to the reflectivity

$$r_2(x_0,L)=\frac{B(x_0)}{A(x_0)}=e^{-2i\delta x_0}\frac{v\sinh[S(L-x_0)]}{(u-i\delta)\sinh[S(L-x_0)]-S\cosh[S(L-x_0)]}. \tag{11}$$

It should be noted that, as seen from their definitions, the above reflectivities Eqs. (10) and (11) include the propagation phase.

With the obtained reflectivities for the two types of boundary conditions, it is easy to derive the laser threshold condition for each circular Bragg laser configuration.

1. Circular DFB laser:

The limiting cases $r_1(x_b) \to \infty$ or $r_2(0, x_b) = 1$ lead to the same result

$$\tanh[Sx_b] = \frac{S}{u - v - i\delta}. \tag{12}$$

2. Disk Bragg laser:

Considering the radially propagating waves in the disk and taking the unity reflectivity at the center, the threshold condition is $1 \cdot e^{2g_A x_0} \cdot r_2(x_0, x_b) = 1$, which reads

$$\frac{e^{2(g_A - i\delta)x_0} \cdot v \cdot \sinh[S(x_b - x_0)]}{(u - i\delta)\sinh[S(x_b - x_0)] - S\cosh[S(x_b - x_0)]} = 1. \tag{13}$$

3. Ring Bragg laser:

Considering the radially propagating waves in the annular defect, the threshold condition is $r_1(x_L) \cdot e^{2g_A(x_R - x_L)} \cdot r_2(x_R, x_b) = 1$, which reads

$$\frac{(u - v - i\delta)\sinh[Sx_L] + S\cosh[Sx_L]}{-(u - v - i\delta)\sinh[Sx_L] + S\cosh[Sx_L]} \cdot \frac{e^{2(g_A - i\delta)(x_R - x_L)} \cdot v \cdot \sinh[S(x_b - x_R)]}{(u - i\delta)\sinh[S(x_b - x_R)] - S\cosh[S(x_b - x_R)]} = 1. \tag{14}$$

The above threshold conditions Eqs. (12), (13), and (14) govern the modes of the lasers of each type and will be used to obtain their threshold gains (g_A) and corresponding detuning factors (δ). With these values, substituting Eqs. (4), (5), (8), and (9) into Eq. (1) and then matching them at the interfaces yield the corresponding in-plane modal field patterns. Despite their much simpler and more direct forms, these threshold conditions automatically satisfy the requirements that $E(x)$ and $E'(x)$ be continuous at every interface between the grating and no-grating regions (Sun & Yariv, 2009c).

2.2 Numerical mode solving method

When solving the modes at threshold with uniform gain (or pump) distribution across the device, g_A is independent of x so that Eqs. (2) and (3) can have analytical solutions Eqs. (4) and (5), or (8) and (9). In the case of using a nonuniform pump profile and/or taking into account the gain saturation effect in above-threshold operation, g_A becomes dependent on x and Eqs. (2) and (3) have to be solved numerically. The modes are then obtained by identifying those satisfying the boundary conditions.

As explained in Sec. 2.1, the same boundary conditions (BCs) apply to all the three types of circular Bragg lasers: (i) $A(0) = B(0)$; (ii) $B(x_b) = 0$; (iii) $A(x)$ and $B(x)$ continuous for $0 < x < x_b$. In Eqs. (2) and (3), $g_0(x)$ for a certain gain distribution profile can be parameterized with a proportionality constant, say, its maximal value g_0.

The mode solving procedure is as follows: Having BC(i), we start with an amplitude set $[A\ B] = A(0)[1\ 1]$ at the center, then numerically integrate Eqs. (2) and (3) along x to the exterior boundary x_b, during which both A and B values are kept continuous at every interface between grating and no-grating regions to satisfy BC(iii). After the integration, we have $B(x_b)$ whose absolute value marks a contour map in the 2-D plane of g_0 and δ. Now each minimum point in this contour map satisfies BC(ii) and thus represents a mode with corresponding g_0 and δ. Retrieving $A(x)$ and $B(x)$ for this mode and substituting them into Eq. (1) give the modal field pattern.

We can also calculate the modal pump level using the obtained g_0. Assuming a linear pump–gain relationship above transparency, the unsaturated gain $g_0(x)$ follows the profile of pump intensity $I_{\text{pump}}(x)$, and we may define the pump level $P_{\text{pump}} \equiv \int I_{\text{pump}}(x) \cdot 2\pi\rho \cdot \mathrm{d}\rho =$

$P_0 \int g_0(x) \cdot x \cdot \mathrm{d}x$, where P_0 having a power unit is a proportionality constant determined by specific experimental setup. For simple $g_0(x)$ profiles, P_{pump} can have analytical expressions as will be shown in Sec. 4.2, otherwise, numerical integration always remains a resort.

2.3 Mode-solving accuracy check

In this subsection we derive an energy relation on which the examination of mode-solving accuracy is based. This energy relation is a direct result of the coupled-mode equations (2) and (3) combined with the boundary conditions and thus is exact.

Similar to the procedure in (Haus, 1975), multiplying Eq. (2) by A^* and Eq. (3) by B^*, then adding each equation to its complex conjugate, one obtains

$$\frac{\mathrm{d}|A|^2}{\mathrm{d}x} = 2\left(g_A - h_{1r}\right)|A|^2 - v \cdot A^* B \cdot e^{2i\delta x} - v^* \cdot AB^* \cdot e^{-2i\delta x}, \tag{15}$$

$$\frac{\mathrm{d}|B|^2}{\mathrm{d}x} = -2\left(g_A - h_{1r}\right)|B|^2 + v \cdot AB^* \cdot e^{-2i\delta x} + v^* \cdot A^* B \cdot e^{2i\delta x}. \tag{16}$$

Subtracting Eq. (16) from Eq. (15) yields

$$\frac{\mathrm{d}}{\mathrm{d}x}\left(|A|^2 - |B|^2\right) = 2g_A\left(|A|^2 + |B|^2\right) - 2h_{1r}\left|Ae^{-i\delta x} + Be^{i\delta x}\right|^2. \tag{17}$$

Integrating Eq. (17) from $x = 0$ to $x = x_b$ and applying the boundary conditions $A(0) = B(0)$ and $B(x_b) = 0$ lead to

$$\underbrace{|A(x_b)|^2}_{\text{peripheral leakage}} + \underbrace{2h_{1r}\int_{\text{grating}}\left|Ae^{-i\delta x} + Be^{i\delta x}\right|^2 \mathrm{d}x}_{\text{vertical laser emission}} = \underbrace{2\int_0^{x_b} g_A\left(|A|^2 + |B|^2\right)\mathrm{d}x}_{\text{power generated in the gain medium}}, \tag{18}$$

which is interpreted as the energy conservation theorem for the surface-emitting circular Bragg lasers. This equation states that, in steady state, the net power generated in the gain medium is equal to the sum of peripheral leakage power and vertical emission power. Due to its exactness, we may use this relation to monitor the accuracy of mode solving by substituting into Eq. (18) the obtained modal $g_0(x)$, δ, $A(x)$, and $B(x)$ and comparing the left-hand and right-hand sides of the equation.

As an aside, it should be noted that all the power terms in Eq. (18) are in units of a saturation power defined by

$$P_{\text{sat}} \equiv E_{\text{sat}}^2\, 4D/\beta, \tag{19}$$

where E_{sat} is the saturation field which relates to the saturation intensity by $I_{\text{sat}} = cn\varepsilon_0|E_{\text{sat}}|^2/2$ (c, the speed of light; n, transverse effective index; ε_0, the vacuum permittivity), and D is the thickness (vertical dimension) of the laser resonator.

3. Near-threshold modal properties

3.1 Threshold, frequency detuning, and in-plane modal pattern

For numerical demonstration, we assume all the lasers possess a vertical layer structure as described in (Scheuer et al., 2005a) which was designed for 1.55 μm laser emission. The

grating design procedure is detailed in Appendix B. The effective index n_{eff} is calculated to be 2.83 and the in-plane propagation constant $\beta = k_0 n_{\text{eff}} = 11.47\ \mu\text{m}^{-1}$. The circular grating is designed to follow the phase of Hankel functions with $m = 0$ to favor circularly symmetric modes. A quarter duty cycle is chosen to have both large feedback for in-plane waves while keeping a considerable amount of vertical emission. The coupling coefficients were found to be $h_1 = 0.0072 + 0.0108i$ and $h_2 = 0.0601$.

Since we would like to compare the modal properties of different types of lasers with a same footprint, a typical device size of $x_b = 200$ (corresponding to $\rho_b \approx 17.4\ \mu\text{m}$) is assumed for all. For the disk Bragg laser, the inner disk radius x_0 is assumed to be $x_b/2 = 100$. For the ring Bragg laser, the annular defect is assumed to be located at the middle $x_b/2 = 100$ and the defect width is set to be a wavelength of the cylindrical waves therein, yielding $x_L + x_R = x_b = 200$ and $x_R - x_L = 2\pi$. The calculated modal field patterns, along with the corresponding threshold gain values (g_A) and frequency detuning factors (δ), of the circular DFB, disk, and ring Bragg lasers are listed in Table 1.

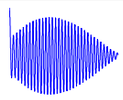
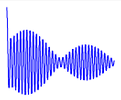
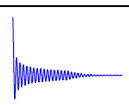
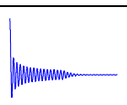
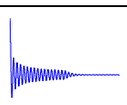
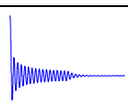
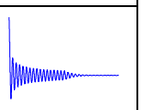
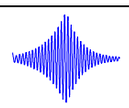
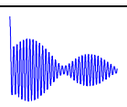
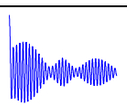
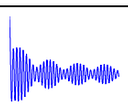
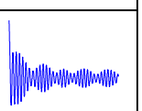
Mode number		1	2	3	4	5
Circular DFB laser	Modal field					
	g_A (10^{-3})	0.283	1.03	2.04	3.11	4.12
	δ (10^{-3})	61.8	66.6	74.1	83.6	94.6
Disk Bragg laser	Modal field					
	g_A (10^{-3})	0.127	0.288	0.454	0.690	1.21
	δ (10^{-3})	49.8	21.2	–8.09	–37.4	–66.5
Ring Bragg laser	Modal field					
	g_A (10^{-3})	0.457	1.06	1.92	3.14	4.09
	δ (10^{-3})	55.9	66.9	71.0	84.4	91.6

Table 1. Modal field patterns, along with their threshold gains (g_A) and frequency detuning factors (δ), of the circular DFB, disk, and ring Bragg lasers. All the three types of lasers have an exterior boundary radius of $x_b = 200$. After (Sun & Yariv, 2008)

A comparison of these modal properties concludes the following features of the three laser structures:

1. All the displayed modes of the circular DFB laser are in-band modes on one side of the band gap (all $\delta > 0$). This is due to the radiation coupling induced mode selection mechanism (Sun & Yariv, 2007). Increased gain results in the excitation of higher-order modes.
2. All the displayed modes of the disk Bragg laser are confined to the center disk with negligible peripheral power leakage and thus possess very low thresholds and very small modal volumes as will be shown in Sec. 3.3.

3. All the displayed modes of the ring Bragg laser, with the exception of the fundamental defect mode, resemble their counterparts of the circular DFB laser. The defect mode has a larger threshold gain than the fundamental mode of the circular DFB laser, but the former possesses a much higher emission efficiency as will be shown in Sec. 3.3.

3.2 Radiation field and far-field pattern

As mentioned earlier, by implementing a second-order circular grating design, the gratings can not only provide feedback for the in-plane fields but also couple the laser emission vertically out of the resonator plane. As derived in Appendix A, Eq. (A12) relates the in-plane fields with the vertical radiation field in the grating regions. The radiation pattern at the emission surface is known as the near-field. For the grating design with $m = 0$, the near-field is expressed as

$$\Delta E = \left(s_1 A e^{-i\delta x} + s_{-1} B e^{i\delta x}\right)\left|H_0^{(1)}\right|, \tag{20}$$

where s_1 and s_{-1} at the emission surface can be obtained numerically according to Eq. (A13) for a given grating structure. Following the design procedure in Appendix B, both s_1 and s_{-1} at the emission surface were calculated to be $0.1725 - 0.0969i$. Using the Huygens–Fresnel principle, the diffracted far-field radiation pattern of light from a circular aperture can be calculated under the parallel ray approximation ($|\mathbf{r}| \gg |\mathbf{r}'|$) (Hecht, 1998):

$$\begin{aligned} U(\mathbf{r}) &\propto \iint_{\text{aperture}} \Delta E(\rho,\varphi)\frac{\exp\left(ik\left|\mathbf{r}-\mathbf{r}'\right|\right)}{4\pi\left|\mathbf{r}-\mathbf{r}'\right|}\mathrm{d}\mathbf{r}' \approx \frac{e^{ikr}}{4\pi r}\iint_{\text{aperture}} \Delta E(\rho,\varphi)\exp\left(-ik(\mathbf{r}'\cdot\hat{\mathbf{r}})\right)\mathrm{d}\mathbf{r}' \\ &= \frac{e^{ikr}}{4\pi r}\int_{\varphi=0}^{2\pi}\int_{\rho=0}^{\rho_b}\Delta E(\rho)\exp\left[-ik\rho\sin\theta\cos(\varphi-\phi)\right]\rho\mathrm{d}\rho\mathrm{d}\varphi = \frac{e^{ikr}}{2r}\int_0^{\rho_b}\Delta E(\rho)J_0(k\rho\sin\theta)\rho\mathrm{d}\rho, \end{aligned} \tag{21}$$

where

$$\mathbf{r}' = \rho\cos\varphi\hat{\mathbf{x}} + \rho\sin\varphi\hat{\mathbf{y}}$$

is the source point and

$$\mathbf{r} = r\sin\theta\cos\phi\hat{\mathbf{x}} + r\sin\theta\sin\phi\hat{\mathbf{y}} + r\cos\theta\hat{\mathbf{z}}$$

is the field point. The far-field intensity pattern is then given by

$$I(\mathbf{r}) = U^*(\mathbf{r})U(\mathbf{r}) = \left|U(\mathbf{r})\right|^2 \tag{22}$$

and plotted in Fig. 3 for the fundamental mode of circular DFB, disk, and ring Bragg lasers.

In the far-field patterns, the different lobes correspond to different diffraction orders of the light emitted from the circular aperture. In the circular DFB and ring Bragg lasers, most of the energy is located in the first-order Fourier component thus their first-order diffraction peaks dominate. In the disk Bragg laser it is obvious that the zeroth-order peak dominates. These calculation results are similar to some of the experimental data for circular DFB and DBR lasers (Fallahi et al., 1994; Jordan et al., 1997).

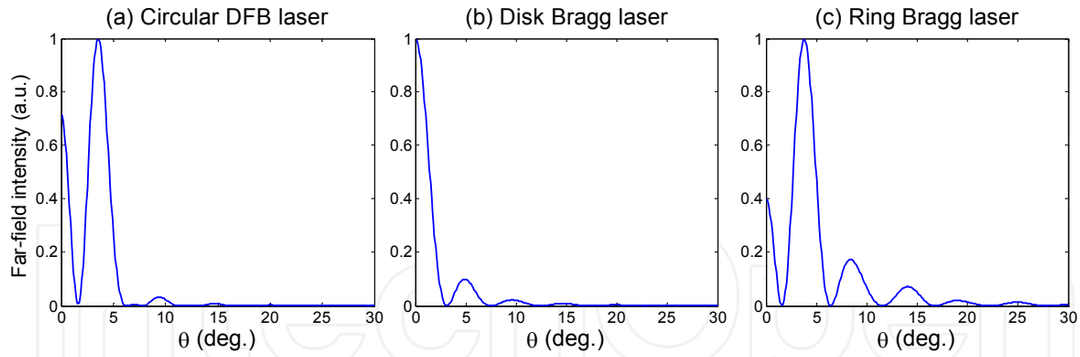


Fig. 3. Far-field intensity patterns of the fundamental mode of (a) circular DFB, (b) disk, and (c) ring Bragg lasers. After (Sun & Yariv, 2009a)

3.3 Single-mode range, quality factor, modal area, and internal emission efficiency

In the previous subsections we have compared the modal properties for devices with a fixed exterior boundary radius x_b = 200. In what follows we will vary the device size and investigate the size dependence of modal gains to determine the single-mode range for each laser type. Within each own single-mode range limit, the fundamental mode of these lasers will be used to calculate and compare the quality factor, modal area, and internal emission efficiency. Similar to the prior calculations with a fixed x_b, we still keep $x_0 = x_b/2$ for the disk Bragg laser and $x_L + x_R = x_b$, $x_R - x_L = 2\pi$ for the ring Bragg laser even as x_b varies.

Single-Mode Range

In the circular Bragg lasers, since a longer radial Bragg grating can provide stronger feedback for in-plane waves, larger devices usually require a lower threshold gain. The downside is that a larger size also results in smaller modal discrimination, which is unfavorable for single-mode operation in these lasers. As a result, there exists a range of the exterior boundary radius x_b values for each laser type within which range the single-mode operation can be achieved. This range is referred to as the "single-mode range." Figure 4 plots the evolution of threshold gains for the 5 lowest-order modes as x_b varies from 50 to 350. The single-mode ranges for the circular DFB, disk, and ring Bragg lasers are 50–250, 60–140, and 50–250, respectively, which are marked as the pink regions. Since single-mode

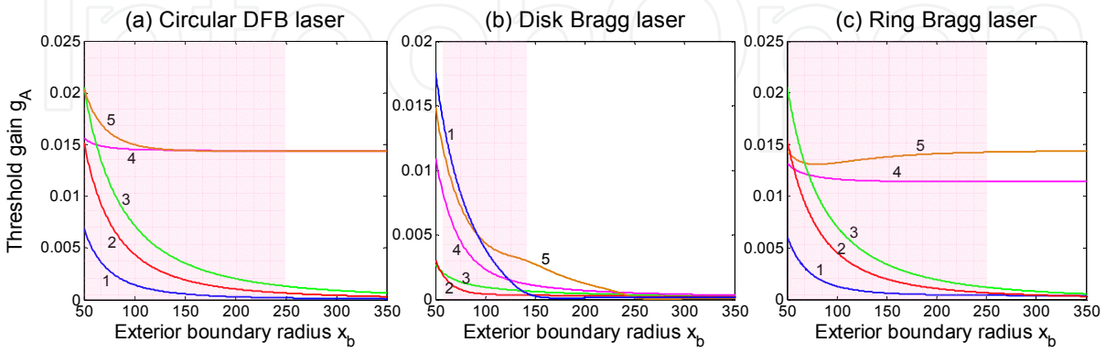


Fig. 4. Evolution of threshold gains of the 5 lowest-order modes of (a) circular DFB, (b) disk, and (c) ring Bragg lasers. The modes are labeled in accord with those shown in Table 1. The single-mode range for each laser type is marked in pink. After (Sun & Yariv, 2008)

operation is usually preferred in laser designs, in the rest of this subsection we will limit x_b to remain within each single-mode range and focus on the fundamental mode only.

Quality Factor

As a measure of the speed with which a resonator dissipates its energy, the quality factor Q for optical resonators is usually defined as $\omega\mathcal{E}/P$ where ω denotes the radian resonance frequency, $\mathcal{E}$ the total energy stored in the resonator, and P the power loss. In our surface-emitting circular Bragg lasers, the power loss P has two contributions: coherent vertical laser emission coupled out of the resonator due to the first-order Bragg diffraction, and peripheral power leakage due to the finite radial length of the Bragg reflector.

Jebali et al. recently developed an analytical formalism to calculate the Q factor for first-order circular grating resonators using a 2-D model in which the in-plane peripheral leakage was considered as the only source of power loss (Jebali et al., 2007). To include the vertical emission as another source of the power loss, a rigorous analytical derivation of the Q factor requires a 3-D model be established. This is much more complicated than the 2-D case. However, since we are interested in comparing different laser types, a relative Q value will be good enough. Considering that the energy stored in a volume is proportional to $\int |\mathbf{E}|^2 \, \mathrm{d}V$ and that the outflow power through a surface is proportional to $\int |\mathbf{E}|^2 \, \mathrm{d}S$, we define an unnormalized quality factor

$$Q' = \frac{\int_0^D \mathrm{d}z \int_0^{2\pi} \mathrm{d}\varphi \int_0^{\rho_b} |E(\rho,z)|^2 \, \rho \mathrm{d}\rho}{\iint\limits_{\text{grating}} |\Delta E(\rho, z=0)|^2 \, \rho \mathrm{d}\rho \mathrm{d}\varphi + \int_0^D \mathrm{d}z \int_0^{2\pi} |E(\rho=\rho_b, z)|^2 \, \rho_b \mathrm{d}\varphi} \tag{23}$$

$$= \frac{\int_0^D Z^2(z)\mathrm{d}z \cdot \int_0^{x_b} |E(x)|^2 \, x \mathrm{d}x}{\int\limits_{\text{grating}} |\Delta E(x, z=0)|^2 \, x \mathrm{d}x + \int_0^D Z^2(z)\mathrm{d}z \cdot |E(x=x_b)|^2 \, \beta x_b},$$

where $Z(z)$ denotes the vertical mode profile for a given layer structure [see Eq. (A3)] and D the thickness of the laser resonator. For a circularly symmetric mode, the angular integration factors are canceled out. The expressions for the in-plane field E and radiation field ΔE are given by Eqs. (1) and (20), respectively.

The unnormalized quality factor Q' Eq. (23) is obviously proportional to an exact Q and the former is more intuitive and convenient for calculational purposes. The Q' of the fundamental mode for the three laser types is calculated and displayed in Fig. 5. As expected, increase in the device size (x_b) results in an enhanced Q' value for all three types of lasers. Additionally, the disk Bragg laser exhibits a much higher Q' than the other two laser structures of identical dimensions. As an example, for x_b = 100, the Q' value of the disk Bragg laser is approximately 3 times greater than that of the circular DFB or ring Bragg lasers. This is consistent with their threshold behaviors shown in Table 1.

Modal Area

Based on the definition of modal volume (Coccioli et al., 1998), an effective modal area is similarly defined:

$$A_{\text{mode}}^{\text{eff}} = \frac{\iint |\mathbf{E}|^2 \, x \mathrm{d}x \mathrm{d}\varphi}{\max\{|\mathbf{E}|^2\}}. \tag{24}$$

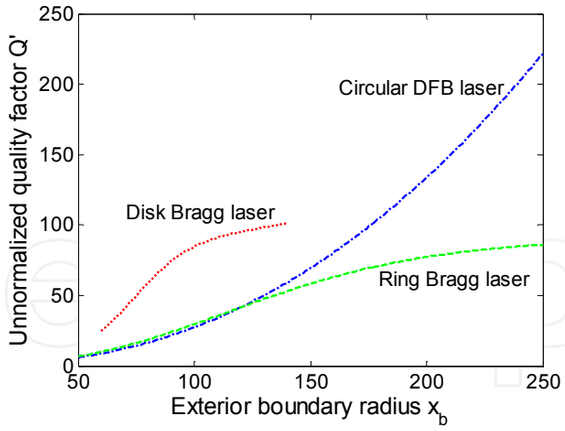


Fig. 5. Unnormalized quality factor of circular DFB, disk, and ring Bragg lasers. After (Sun & Yariv, 2008)

The modal area is a measure of how the modal field is distributed within the resonator. A highly localized mode having a small modal area can have strong interaction with the emitter. Figure 6 plots $A_{\text{mode}}^{\text{eff}}$ of the fundamental mode, within each single-mode range, for the three laser types. The top surface area of the laser resonator (πx_b^2) is also plotted to serve as a reference. The modal area of the disk Bragg laser is found to be at least one order of magnitude lower than those of the circular DFB and ring Bragg lasers. This is not surprising and can be inferred from their unique modal profiles listed in Table 1.

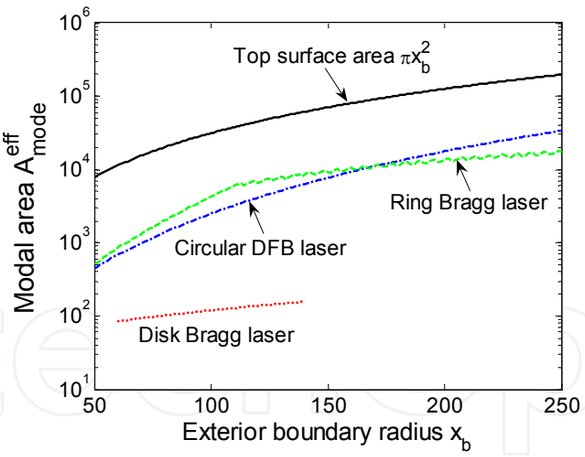


Fig. 6. Modal area of circular DFB, disk, and ring Bragg lasers. The top surface area of the laser resonator (πx_b^2) is also plotted as a reference. After (Sun & Yariv, 2008)

Internal Emission Efficiency

As mentioned earlier, the generated net power in the circular Bragg lasers is dissipated by two kinds of loss: vertical laser emission and peripheral power leakage. The internal emission efficiency η_{in} is thus naturally defined as the fraction of the total power loss which is represented by the useful vertical laser emission. Figure 7 depicts the η_{in} of the fundamental mode, within each single-mode range, for the three laser types. As expected,

all the lasers possess a larger η_{in} with a larger device size. Comparing devices of identical dimensions, only the disk and ring Bragg lasers achieve high emission efficiencies. This is a result of their fundamental modes being located in a band gap while the circular DFB laser's fundamental mode is at a band edge, i.e., in a band. Band-gap modes experience much stronger reflection from the Bragg gratings, yielding less peripheral power leakage than in-band modes.

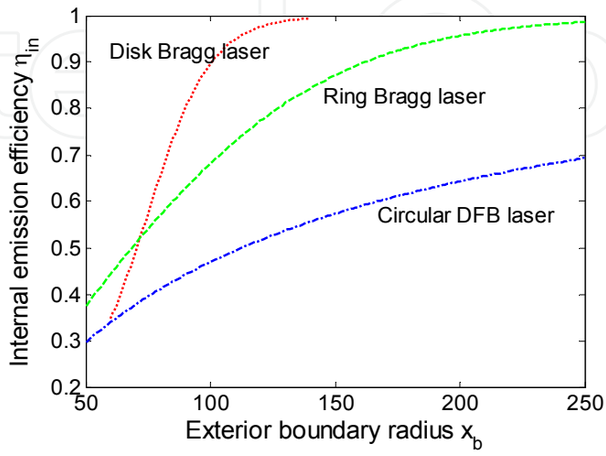


Fig. 7. Internal emission efficiency of circular DFB, disk, and ring Bragg lasers. After (Sun & Yariv, 2008)

Summary of Comparison

In this subsection, by varying the device size we have obtained the single-mode range and compared the quality factor, modal area, and internal emission efficiency of the three types of lasers. It is demonstrated that, under similar conditions, disk Bragg laser has the highest quality factor, the smallest modal area, and the highest internal emission efficiency, indicating its suitability in high-efficiency, low-threshold, ultracompact laser design, while ring Bragg laser has a large single-mode range, large modal area, and high internal emission efficiency, indicating its wide application as a high-efficiency, large-area laser.

4. Above-threshold modal analysis

In Sec. 3 we have solved the modes and compared the near-threshold modal properties of the three types of surface-emitting circular Bragg lasers. This section focuses on an above-threshold modal analysis which includes gain saturation effect. The coupled-mode equations (2) and (3) will be solved numerically with boundary conditions. The relation of surface emission power versus pump power will be simulated. The laser threshold and external emission efficiency will be compared for these lasers under different pump profiles. Lastly, with the device size varying in a large range, the evolution curve of pump level for several lowest-order modes will be generated and the optimal design guidelines for these lasers will be suggested.

4.1 Surface emission power versus pump power relation

The numerical mode solving recipe is described in detail in Sec. 2.2. Simply put, Eqs. (2) and (3) are integrated along x from $x = 0$ to $x = x_b$ with the initial boundary condition $[A\ B] =$

$A(0)$[1 1]. By identifying those satisfying the final boundary condition $B(x_b) = 0$ one finds the modes with corresponding g_0 and δ. The modal pump level is then given by $P_{\text{pump}} = \int g_0(x) \cdot x \cdot \mathrm{d}x$ in units of a proportionality constant P_0. Explained in Sec. 2.3, the surface emission power P_{em} from the laser is just the second term on the left-hand side of Eq. (18). By varying the value of $A(0)$ at the beginning of the integration process, we are able to get the (P_{pump}, P_{em}) pairs which basically form the typical input–output relation for a laser mode.

As an example, we consider the circular DFB laser with $x_b = 200$ and the other structural parameters the same as those used in Sec. 3. The additional parameter used in the numerical integration, the nonsaturable internal loss α, is assumed to be 0.2×10^{-3} (already normalized by β) for typical III–V quantum well lasers. With the simulated (P_{pump}, P_{em}) pairs, the typical laser input–output relation is obtained for the fundamental mode and plotted in Fig. 8. The laser threshold P_{th} is defined as the pump level at the onset of surface laser emission. The external emission efficiency (or, energy conversion efficiency) η_{ex} is defined as the slope $\mathrm{d}P_{\text{em}}/\mathrm{d}P_{\text{pump}}$ of the linear fit of the simulated data points up to $P_{\text{em}} = 10P_{\text{sat}}$. As can be seen, the output power varies linearly with the pump power above threshold, which is in agreement with the theoretical and experimental results for typical laser systems [see, e.g., Sec. 9.3 of (Yariv, 1989)].

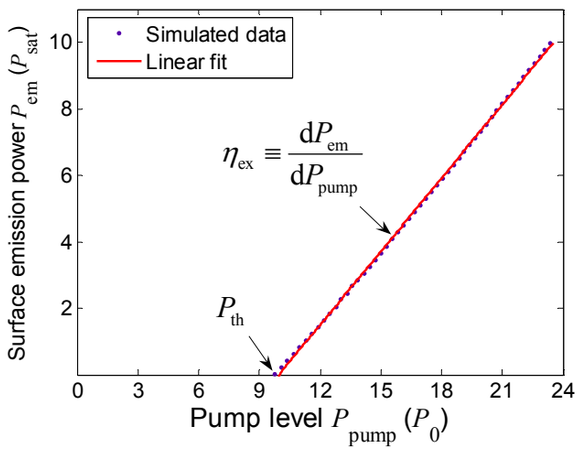


Fig. 8. Surface emission power P_{em} (in units of P_{sat}) versus pump power level P_{pump} for the fundamental mode of circular DFB laser ($x_b = 200$) under uniform pumping. The laser threshold P_{th} is defined as the pump level at the onset of surface laser emission. The external emission efficiency η_{ex} is defined as the slope of the linear fit of the simulated data points up to $P_{\text{em}} = 10P_{\text{sat}}$.

4.2 Nonuniform pumping effects

So far our studies on the circular Bragg lasers have assumed a uniform pumping profile and thus a uniform gain distribution across the devices. In practical situations, the pumping profile is usually nonuniform, distributed either in a Gaussian shape in optical pumping (Olson et al., 1998; Scheuer et al., 2005a) or in an annular shape in electrical pumping (Wu et al., 1994). The effects of nonuniform pumping have been investigated theoretically (Kasunic et al., 1995; Greene & Hall, 2001) and experimentally (Turnbull et al., 2005) for circular DFB lasers. In this subsection we will study and compare the nonuniform effects on the three types of surface-emitting circular Bragg lasers.

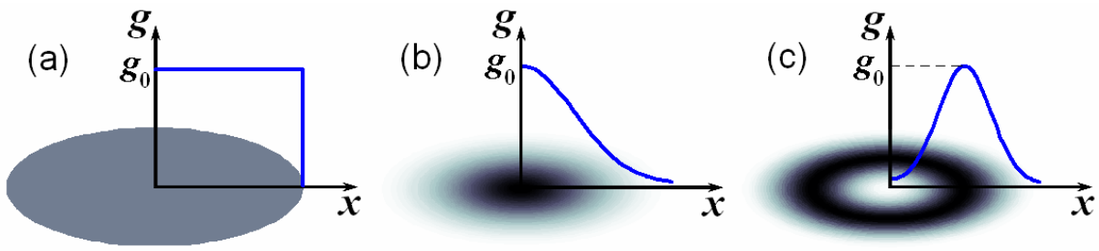


Fig. 9. Illustration of different pump profiles: (a) uniform; (b) Gaussian; (c) annular

Let us focus on three typical pumping profiles – uniform, Gaussian, and annular – as shown in Fig. 9. The pump level P_{pump} can be expressed analytically in terms of the pump profile parameters:

a. Uniform:

$$g_0(x) = g_0,\ 0 \le x \le x_b,\ P_{\text{pump}} = \int_0^{x_b} g_0 \cdot x \cdot \mathrm{d}x = \tfrac{1}{2} g_0 x_b^2, \tag{25}$$

b. Gaussian:

$$g_0(x) = g_0 \exp\left(-\tfrac{x^2}{w_p^2}\right),\ x \ge 0,\ P_{\text{pump}} = \int_0^{\infty} g_0 \exp\left(-\tfrac{x^2}{w_p^2}\right) \cdot x \cdot \mathrm{d}x = \tfrac{1}{2} g_0 w_p^2, \tag{26}$$

c. Annular:

$$g_0(x) = g_0 \left[\exp\left(-\tfrac{(x-x_p)^2}{w_p^2}\right) + \exp\left(-\tfrac{(x+x_p)^2}{w_p^2}\right)\right],\ x \ge 0,$$

$$P_{\text{pump}} = \int_0^{\infty} g_0 \left[\exp\left(-\tfrac{(x-x_p)^2}{w_p^2}\right) + \exp\left(-\tfrac{(x+x_p)^2}{w_p^2}\right)\right] \cdot x \cdot \mathrm{d}x = g_0 \left[w_p^2 \exp\left(-\tfrac{x_p^2}{w_p^2}\right) + \sqrt{\pi} w_p x_p \operatorname{erf}\left(\tfrac{x_p}{w_p}\right)\right], \tag{27}$$

where the error function $\operatorname{erf}(x) \equiv \frac{2}{\sqrt{\pi}} \int_0^x \exp(-t^2)\, \mathrm{d}t$.

To compare the nonuniform pumping effects, the typical exterior boundary radius x_b = 200 is again assumed for all the circular DFB, disk, and ring Bragg lasers. In addition, for the disk Bragg laser the inner disk radius is set to be $x_0 = x_b/2$, and for the ring Bragg laser the two interfaces separating the grating and no-grating regions are located at $x_L = x_b/2 - \pi$ and $x_R = x_b/2 + \pi$. Following the calculation procedure in Sec. 4.1, the threshold pump level P_{th} and the external emission efficiency η_{ex} of the fundamental mode of the three types of lasers were calculated with the uniform, Gaussian, and annular pump profiles, respectively, and the results are listed in Table 2. Without loss of generality, the Gaussian profile was assumed to follow Eq. (26) with $w_p = x_b/2 = 100$, and the annular profile was assumed to follow Eq. (27) with $x_p = x_b/2 = 100$ and $w_p = x_b/4 = 50$. The numbers shown in Table 2 indicate an inverse relation between P_{th} and η_{ex}. The lowest P_{th} and the highest η_{ex} are achieved with the Gaussian pump for the circular DFB and disk Bragg lasers and with the annular pump for the ring Bragg laser.

These observations can actually be understood with fundamental laser physics: In any laser system the overlap factor between the gain spatial distribution and that of the modal intensity is crucial and proportionate. In semiconductor lasers once the pump power is strong enough to induce the population inversion the medium starts to amplify light. The lasing threshold is determined by equating the modal loss with the modal gain, which is the

Pump profile	Circular DFB laser		Disk Bragg laser		Ring Bragg laser	
	P_{th}	η_{ex}	P_{th}	η_{ex}	P_{th}	η_{ex}
Uniform	9.760	0.7369	6.565	0.4374	13.162	0.9278
Gaussian	5.967	0.9961	2.373	0.8741	8.570	1.379
Annular	6.382	0.9742	5.855	0.7358	7.010	1.500

Table 2. Threshold pump level P_{th} (in units of P_0) and external emission efficiency η_{ex} (in units of P_{sat}/P_0) of circular DFB, disk, and ring Bragg lasers under different pump profiles. After (Sun & Yariv, 2009b)

exponential gain constant experienced by the laser mode. This modal gain is proportional to the overlap integral between the spatial distribution of the gain and that of the modal intensity. Therefore if one assumes that, to the first order, the gain is proportional to the excess pump power over the transparency, then the threshold pump level P_{th} is inversely proportional to the above overlap integral [see, e.g., Sec. 11.3 of (Yariv, 1989)]. On the other hand, since the rate of simulated emission per electron and thus the gain are proportional to the modal intensity as seen by the electron [see, e.g., Sec. 8.3 of (Yariv, 1989)], this leads to a direct proportion between the external emission efficiency η_{ex} and the overlap integral. The bottom line is that a larger overlap between the pump profile and the modal intensity distribution results in more efficient energy conversion in the gain medium which consequently leads to a lower P_{th} and a higher η_{ex}.

4.3 Considerations in optimal design

To obtain the optimal design for these circular Bragg lasers, we will again vary their device size in a large range and inspect their size-dependent behavior. Like what we have done in Sec. 3.3, we will vary the exterior boundary radius x_b for all the lasers while keeping $x_0 = x_b/2$ for the disk Bragg laser and $x_L = x_b/2 - \pi$, $x_R = x_b/2 + \pi$ for the ring Bragg laser.

Figure 10 shows the dependence of the pump level P_{pump} and the frequency detuning factor δ on the device size x_b for the 3 lowest-order modes, under uniform pump profile, of the three types of lasers. In each subfigure, the modes are numbered in accord with those shown in Table 1. For both P_{pump} and δ, dashed lines mark their values obtained at threshold and solid lines at $P_{em} = 10P_{sat}$.

Seen from the upper left and right subplots of Fig. 10, the circular DFB and ring Bragg lasers still possess large discrimination between the modes even when operated in above-threshold regime (e.g., at $P_{em} = 10P_{sat}$), which ensures them a large single-mode range of at least 50–250. Additionally, we have identified low-pump ranges for their Mode 1 at $P_{em} = 10P_{sat}$, which are 100–160 for the circular DFB laser and 80–130 for the ring Bragg laser. The low-pump range is another important factor in designing such lasers for high-efficiency, high-power applications. The existence of this low-pump range is a result of competition between the pumped area and the required gain level: although larger devices require a larger area to be pumped, their longer radial Bragg gratings reduce the needed gain because of stronger reflection of the optical fields from the gratings.

Seen from the upper middle subplot of Fig. 10, the P_{pump} for the disk Bragg laser exhibits interesting behaviors: (i) at $x_b = 200$, the order of Modes 1 and 2 exchanges from at threshold to above threshold due to the gain saturation effects; (ii) the single-mode range (for Mode 2) shifts from 60–140 at threshold to 90–175 at high surface emission level $P_{em} = 10P_{sat}$. Therefore the single-mode range for designing the disk Bragg laser should be the overlap of these two ranges, i.e., 90–140.

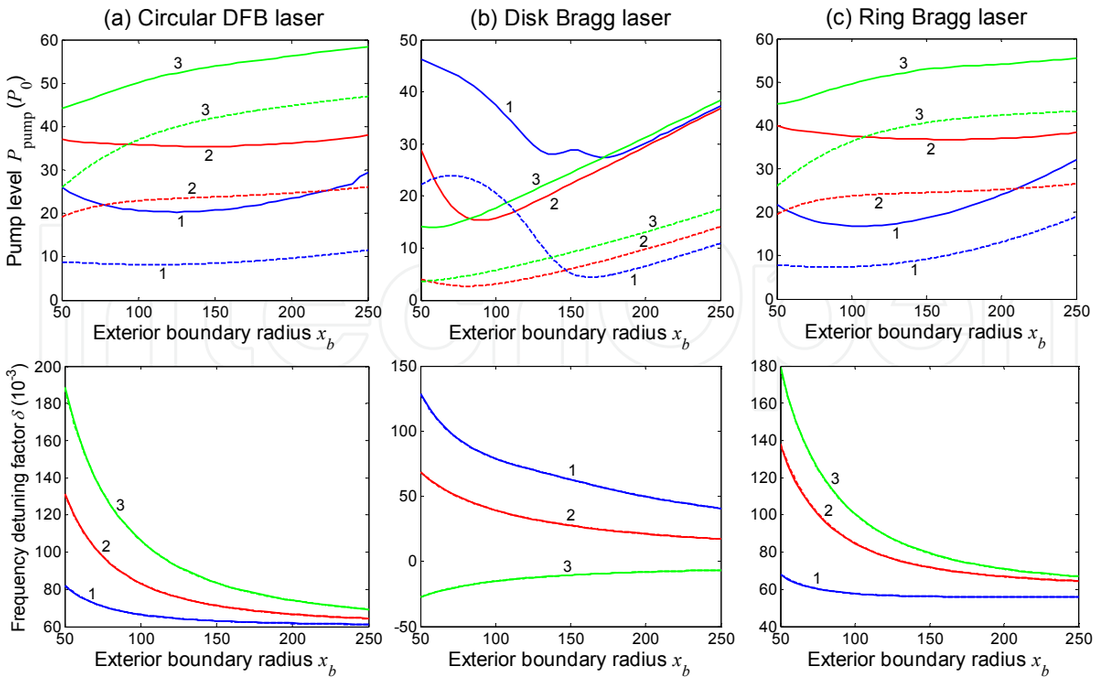


Fig. 10. Device-size-dependent pump level P_{pump} and frequency detuning factor δ of the 3 lowest-order modes, under uniform pump profile, of (a) circular DFB, (b) disk, and (c) ring Bragg lasers. x_b is the exterior boundary radius for all types of lasers. The inner disk radius x_0 of the disk Bragg laser is set to be $x_b/2$. The inner and outer edges of the annular defect of the ring Bragg laser are set to be $x_L = x_b/2 - \pi$ and $x_R = x_b/2 + \pi$, respectively. The modes are labeled in accord with those shown in Table 1. Dashed lines mark the values obtained at threshold and solid lines at $P_{\text{em}} = 10P_{\text{sat}}$. After (Sun & Yariv, 2009b)

Seen from the lower subplots of Fig. 10, all the laser modes have overlapped dashed and solid lines, which means their frequency detuning factors δ are unaffected by the surface emission level. This is because of δ being an intrinsic property of a laser mode.

5. Conclusion and outlook

In this chapter we have described and analyzed a type of on-chip microlasers whose surface emission is very useful for many applications. The main advantage of these lasers would be the relative high (say, more than tens of mW), single-mode optical power emitted broadside and coupled directly into a fiber or telescopic optics. Other areas of applications that can benefit from such lasers include ultrasensitive biochemical sensing (Scheuer et al., 2005b), all-optical gyroscopes (Scheuer, 2007), and coherent beam combination (Brauch et al., 2000) for high-power, high-radiance sources in communications and display technology. Furthermore, a thorough investigation of such lasers may also lead to a better understanding in designing and fabricating a nanosized analogue, if a surface-plasmon approach is employed.

Throughout this work we have been trying to make a small contribution to understanding of the circular Bragg lasers for their applications as high-efficiency, high-power, surface-emitting lasers. We have covered the basic concepts, calculation methods, near- and above-threshold modal properties, and design strategies for such lasers.

We have studied three typical configurations of such circular Bragg lasers – namely, circular DFB laser, disk Bragg laser, and ring Bragg laser. Following the grating design principle for linear DFB lasers, the gratings of circular Bragg lasers have to be in sync with the phases of optical waves in a circular (or cylindrical) geometry. Since the eigensolutions of wave equation in a circular geometry are Hankel functions, this leads to a varying period of the gratings in radial direction, i.e., radially chirped gratings. To obtain efficient output coupling in vertical direction, a second-order scheme has been employed, and a quarter duty cycle has proved to be a good choice.

After a series of comparison of the modal properties, it becomes clear that disk and ring Bragg lasers have superiority over circular DFB lasers in high-efficiency surface emission. More specifically, disk Bragg lasers are most useful in low-threshold, ultracompact laser design while ring Bragg lasers are excellent candidates for high-power, large-area lasers.

Considering above-threshold operation with a nonuniform pump profile, it has been numerically demonstrated and theoretically explained that a larger overlap between the pump profile and modal intensity distribution leads to a lower threshold and a higher energy conversion efficiency. To achieve the same level of surface emission, disk Bragg laser still requires the lowest pump power, even though its single-mode range is modified because of the gain saturation induced mode transition. Circular DFB and ring Bragg lasers find their low-pump ranges at high surface emission level. These results provide us useful information for designing these lasers for single-mode, high-efficiency, high-power applications.

Looking ahead, there is still more work to be done on this special topic. For example, it would be interesting to further investigate how the grating design effects on the modal far-field pattern and what design results in a pattern having all, or almost all, of the energy located in the zeroth-order lobe with narrow divergence. This will be useful for applications which require highly-directional, narrow-divergence laser beams. On the other hand, since this chapter is mainly theoretical analysis oriented, experimental work, of course, has to develop to verify the theoretical predictions. In the field of optoelectronics, a single-mode, high-power laser having controllable beam shape and compatible with on-chip integration is still being highly sought. Due to the many salient features that have been described, it is our belief that the surface-emitting circular Bragg lasers will take the place of the prevailing VCSELs and make the ideal on-chip light source for next-generation optical communications and many other areas.

Appendix A: Derivation of comprehensive coupled-mode theory for circular grating structure in an active medium

In the case that the polarization effects due to the waveguide structure are not concerned, we can start from the scalar Helmholtz equation for the z component of electric field in cylindrical coordinates

$$\left[\frac{1}{\rho}\frac{\partial}{\partial\rho}\left(\rho\frac{\partial}{\partial\rho}\right)+\frac{1}{\rho^2}\frac{\partial^2}{\partial\varphi^2}+k_0^2n^2(\rho,z)+\frac{\partial^2}{\partial z^2}\right]E_z(\rho,\varphi,z)=0, \tag{A1}$$

where ρ, φ, and z are respectively radial, azimuthal, and vertical coordinates, $k_0 = \omega/c = 2\pi/\lambda_0$ is the wave number in vacuum.

For an azimuthally propagating eigenmode, E_z in a passive uniform medium in which the dielectric constant $n^2(\rho, z) = \varepsilon_r(z)$ can be expressed as

$$E_z(\rho,\varphi,z) = E_z^{(m)}(\rho,z)\exp(im\varphi) = \left[AH_m^{(1)}(\beta\rho) + BH_m^{(2)}(\beta\rho) \right] Z(z)\exp(im\varphi), \tag{A2}$$

with m the azimuthal mode number, $\beta = k_0 n_{\text{eff}}$ the in-plane propagation constant, and $Z(z)$ the fundamental mode profile of the planar slab waveguide satisfying

$$\left(k_0^2 \varepsilon_r(z) + \frac{\partial^2}{\partial z^2} \right) Z(z) = \beta^2 Z(z). \tag{A3}$$

In a radially perturbed gain medium, the dielectric constant can be expressed as $n^2(\rho, z) = \varepsilon_r(z) + i\varepsilon_i(z) + \Delta\varepsilon(\rho, z)$ where $\varepsilon_i(z)$ with $|\varepsilon_i(z)| \ll \varepsilon_r(z)$ represents the medium gain or loss and $\Delta\varepsilon(\rho, z)$ is the perturbation profile which in a cylindrical geometry can be expanded in Hankel-phased plane wave series:

$$\begin{aligned}
\Delta\varepsilon(\rho,z) &= -\Delta\varepsilon_0 \sum_{l=\pm1,\pm2} a_l(z)\exp\left(-il\Phi[H_m^{(1)}(\beta_{\text{design}}\rho)]\right) \\
&= -\Delta\varepsilon_0 \sum_{l=\pm1,\pm2} a_l(z)\exp\left(-il\Phi[H_m^{(1)}(x)]\right)\exp(-il\delta\cdot x) \\
&= -\Delta\varepsilon_0 \left[a_2(z)\frac{H_m^{(2)}}{H_m^{(1)}}e^{-2i\delta\cdot x} + a_{-2}(z)\frac{H_m^{(1)}}{H_m^{(2)}}e^{2i\delta\cdot x} + a_1(z)\frac{H_m^{(2)}}{\left|H_m^{(1)}\right|}e^{-i\delta\cdot x} + a_{-1}(z)\frac{H_m^{(1)}}{\left|H_m^{(1)}\right|}e^{i\delta\cdot x} \right].
\end{aligned} \tag{A4}$$

In the above expression, $a_l(z)$ is the lth-order expansion coefficient of $\Delta\varepsilon(\rho, z)$ at a given z. x is the normalized radial coordinate defined as $x = \beta\rho$. $\delta = (\beta_{\text{design}} - \beta)/\beta$ ($|\delta| \ll 1$), the normalized frequency detuning factor, represents a relative frequency shift of a resonant mode from the designed value.

To account for the vertical radiation, an additional term $\Delta E(x, z)$ is introduced into the modal field so that

$$E_z^{(m)}(x,z) = \left[A(x)H_m^{(1)}(x) + B(x)H_m^{(2)}(x) \right] Z(z) + \Delta E(x,z). \tag{A5}$$

Assuming that the radiation field $\Delta E(x, z)$ has an $\exp(\pm ik_0 z)$ dependence on z in free space, i.e.,

$$\left[\frac{1}{\rho}\frac{\partial}{\partial\rho}\left(\rho\frac{\partial}{\partial\rho} \right) - \frac{m^2}{\rho^2} \right] \Delta E = 0, \tag{A6}$$

substituting Eqs. (A4), (A5), and (A6) into Eq. (A1), introducing the large-radius approximations (Scheuer & Yariv, 2003)

$$\left| \frac{H_m^{(1,2)}(x)}{x} \right| \ll \left| \frac{\mathrm{d}H_m^{(1,2)}(x)}{\mathrm{d}x} \right|, \qquad \frac{\mathrm{d}^n H_m^{(1,2)}(x)}{\mathrm{d}x^n} \approx (\pm i)^n H_m^{(1,2)}(x), \tag{A7}$$

neglecting the second derivatives of $A(x)$ and $B(x)$, and applying the modal solution in the passive unperturbed case, one obtains

$$2iZ\left(\frac{\mathrm{d}A}{\mathrm{d}x}H_m^{(1)}-\frac{\mathrm{d}B}{\mathrm{d}x}H_m^{(2)}\right)+i\frac{k_0^2\varepsilon_i}{\beta^2}\left(AH_m^{(1)}Z+BH_m^{(2)}Z\right)+\frac{1}{\beta^2}\left(k_0^2\varepsilon_r+ik_0^2\varepsilon_i+\frac{\partial^2}{\partial z^2}\right)\Delta E$$
$$=\frac{k_0^2\Delta\varepsilon_0}{\beta^2}\left[a_2\frac{H_m^{(2)}}{H_m^{(1)}}e^{-2i\delta\cdot x}+a_{-2}\frac{H_m^{(1)}}{H_m^{(2)}}e^{2i\delta\cdot x}+a_1\frac{H_m^{(2)}}{\left|H_m^{(1)}\right|}e^{-i\delta\cdot x}+a_{-1}\frac{H_m^{(1)}}{\left|H_m^{(1)}\right|}e^{i\delta\cdot x}\right] \tag{A8}$$
$$\times\left(AH_m^{(1)}Z+BH_m^{(2)}Z+\Delta E\right).$$

The phase-matching condition requires that the source and wave have close phase dependence. Grouping the terms with the same kind of Hankel functions leads to the following set of coupled equations:

$$2i\frac{\mathrm{d}A}{\mathrm{d}x}H_m^{(1)}Z+i\frac{k_0^2\varepsilon_i}{\beta^2}AH_m^{(1)}Z=\frac{k_0^2\Delta\varepsilon_0}{\beta^2}\left(a_{-2}BH_m^{(1)}e^{2i\delta\cdot x}Z+a_{-1}\frac{\Delta E}{\left|H_m^{(1)}\right|}H_m^{(1)}e^{i\delta\cdot x}\right), \tag{A9}$$

$$-2i\frac{\mathrm{d}B}{\mathrm{d}x}H_m^{(2)}Z+i\frac{k_0^2\varepsilon_i}{\beta^2}BH_m^{(2)}Z=\frac{k_0^2\Delta\varepsilon_0}{\beta^2}\left(a_2AH_m^{(2)}e^{-2i\delta\cdot x}Z+a_1\frac{\Delta E}{\left|H_m^{(1)}\right|}H_m^{(2)}e^{-i\delta\cdot x}\right), \tag{A10}$$

$$\left(k_0^2\varepsilon_r+\frac{\partial^2}{\partial z^2}\right)\Delta E=k_0^2\Delta\varepsilon_0\left(a_1A\left|H_m^{(1)}\right|e^{-i\delta\cdot x}Z+a_{-1}B\left|H_m^{(1)}\right|e^{i\delta\cdot x}Z\right). \tag{A11}$$

From Eq. (A11), ΔE can be expressed as

$$\Delta E=\left(s_1Ae^{-i\delta\cdot x}+s_{-1}Be^{i\delta\cdot x}\right)\left|H_m^{(1)}\right|, \tag{A12}$$

where

$$s_l(z)=k_0^2\Delta\varepsilon_0\int_{-\infty}^{+\infty}a_l(z')Z(z')G(z,z')\mathrm{d}z', \tag{A13}$$

and $G(z, z')$ is the Green's function satisfying

$$\left(k_0^2\varepsilon_r(z)+\frac{\partial^2}{\partial z^2}\right)G(z,z')=\delta(z-z'). \tag{A14}$$

Substituting Eq. (A12) into Eqs. (A9) and (A10), multiplying both sides by $Z(z)$, and integrating over z yield

$$\frac{\mathrm{d}A}{\mathrm{d}x}=\left(g_A-h_{-1,1}\right)A-\left(h_{-1,-1}+ih_{-2}\right)Be^{2i\delta\cdot x}, \tag{A15}$$

$$\frac{\mathrm{d}B}{\mathrm{d}x}=-\left(g_A-h_{1,-1}\right)B+\left(h_{1,1}+ih_2\right)Ae^{-2i\delta\cdot x}, \tag{A16}$$

where the gain coefficient

$$g_A\equiv-\frac{k_0^2}{2P\beta^2}\int_{-\infty}^{+\infty}\varepsilon_i(z)Z^2(z)\mathrm{d}z, \tag{A17}$$

the radiation coupling coefficients

$$h_{\pm1,\pm1} \equiv \frac{ik_0^2 \Delta\varepsilon_0}{2P\beta^2} \int_{-\infty}^{+\infty} a_{\pm1}(z) s_{\pm1}(z) Z(z)\,\mathrm{d}z, \tag{A18}$$

the feedback coupling coefficients

$$h_{\pm2} \equiv \frac{k_0^2 \Delta\varepsilon_0}{2P\beta^2} \int_{-\infty}^{+\infty} a_{\pm2}(z) Z^2(z)\mathrm{d}z, \tag{A19}$$

and the normalization constant

$$P \equiv \int_{-\infty}^{+\infty} Z^2(z)\mathrm{d}z. \tag{A20}$$

In the case of index grating, we can choose the phase of the grating such that $a_{-1} = a_1$, $a_{-2} = a_2$, then we denote $h_1 = h_{\pm1,\,\pm1}$, $h_2 = h_{\pm2}$. By defining $u = g_A - h_1$ and $v = h_1 + ih_2$, Eqs. (A15) and (A16) become

$$\frac{\mathrm{d}A(x)}{\mathrm{d}x} = u(x)\cdot A(x) - v(x)\cdot B(x)\cdot e^{2i\delta\cdot x}, \tag{A21}$$

$$\frac{\mathrm{d}B(x)}{\mathrm{d}x} = -u(x)\cdot B(x) + v(x)\cdot A(x)\cdot e^{-2i\delta\cdot x}. \tag{A22}$$

Specifically, in the unperturbed (i.e., no-grating) region where $\Delta\varepsilon = 0$, h_1 and h_2 vanish, and Eqs. (A21) and (A22) reduce to

$$\frac{\mathrm{d}A(x)}{\mathrm{d}x} = g_A(x)\cdot A(x), \tag{A23}$$

$$\frac{\mathrm{d}B(x)}{\mathrm{d}x} = -g_A(x)\cdot B(x). \tag{A24}$$

Appendix B: Grating design procedure and calculations of the numerical Green's function $G(z, z')$, coefficients h_1, h_2, and s_1

Since we have previously fabricated such Hankel-phased circular Bragg lasers in InGaAsP active semiconductor material (Scheuer et al., 2005a), we will use the layer structure therein as an example for our numerical study. The target lasing wavelength λ_0 is 1.55 μm. For simplicity, we approximate the complicated layer structure by an effective index profile comprising five layers as illustrated in Table B1. The vertical mode profile $Z(z)$ and the effective index n_{eff} can be obtained numerically using a 1-D mode solver. The effective index n_{eff} was calculated to be 2.83 and the in-plane propagation constant $\beta = k_0 n_{\mathrm{eff}} = 11.47\ \mu\mathrm{m}^{-1}$. Numerical calculations of the mode profile and effective index of the approximated layer structure indicate negligible deviations from those of the exact one.

We focus our analysis on the case of a partially etched grating with an etch depth of 185 nm. The numerical Green's function $G(z, z')$ that satisfies Eq. (A14) with the given layer structure was calculated for $-\infty < z < \infty$ and z' between the top and bottom surfaces of the laser resonator. A surface plot of the real part of $G(z, z')$ is displayed in Fig. B1.

Layer description	Refractive index n	Thickness
Upper cladding	1.54	∞
Third layer	3.281	60.5 nm
Second layer (active region)	3.4057	129 nm
First layer	3.281	60.5 nm
Lower cladding	1.54	∞

Table B1. Approximated layer structure for numerical study

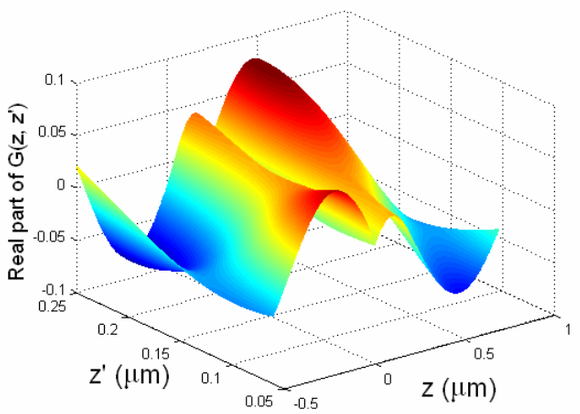


Fig. B1. Real part of the Green's function $G(z, z')$ with $-\infty < z < \infty$ and z' between the top and bottom surfaces of the laser resonator. After (Sun et al., 2008)

To favor a circularly symmetric laser mode, $m = 0$ is specially chosen in the grating phase design. In such case, a Hankel-phased grating modulation with rectangular profile

$$\Theta(\Phi[H_m^{(1)}(x)],\alpha)=\begin{cases}1, & \cos\left(\Phi[H_m^{(1)}(x)]\right)\geq\alpha\\ 0, & \cos\left(\Phi[H_m^{(1)}(x)]\right)<\alpha\end{cases} \tag{B1}$$

can be expanded in Fourier series as

$$\begin{aligned}&\frac{\arccos\alpha}{\pi}+\frac{2}{\pi}\sum_{l=1}^{\infty}\frac{\sin(l\arccos\alpha)}{l}\cos\left(l\Phi[H_m^{(1)}(x)]\right)\\&=\frac{\arccos\alpha}{\pi}+\frac{2}{\pi}\left[\sin(\arccos\alpha)\cos\left(\Phi[H_m^{(1)}(x)]\right)+\frac{\sin(2\arccos\alpha)}{2}\cos\left(2\Phi[H_m^{(1)}(x)]\right)+\cdots\right]\\&=d_c+\frac{1}{2\pi}\sin(2\pi d_c)\left[\exp(-i2\Phi[H_m^{(1)}(x)])+\exp(i2\Phi[H_m^{(1)}(x)])\right]\\&\quad+\frac{1}{\pi}\sin(\pi d_c)\left[\exp(-i\Phi[H_m^{(1)}(x)])+\exp(i\Phi[H_m^{(1)}(x)])\right]+\cdots.\end{aligned} \tag{B2}$$

The expansion yields the coefficients

$$a_2=a_{-2}=\frac{\sin(2\pi d_c)}{2\pi}$$

and

$$a_1 = a_{-1} = \frac{\sin(\pi d_c)}{\pi}$$

where

$$d_c \equiv \frac{\arccos \alpha}{\pi} \quad (-1 < \alpha < 1, \quad 0 < d_c < 1)$$

is the duty cycle of the Hankel-phased rectangular grating. It should be emphasized that the duty cycle has a significant role in determining the coupling coefficients h_1 and h_2 (Barlow et al., 2004). Figure B2 plots h_1 and h_2 as a function of the duty cycle d_c. A judicious choice would be d_c = 0.25 where h_2 is maximal and Re(h_1) is not small so that we can have a large ratio of vertical emission to power leakage, hence a high emission efficiency. Based on Eqs. (A18) and (A19), the grating's coupling coefficients were found to be h_1 = 0.0072 + 0.0108i and h_2 = 0.0601. Calculated from Eq. (A13), s_1 and s_{-1} at the emission surface (i.e., the top surface of the laser resonator) were found to be 0.1725 – 0.0969i.

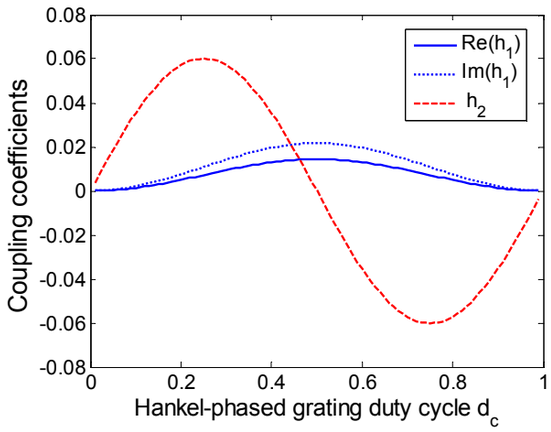


Fig. B2. Radiation coupling coefficient h_1 and feedback coupling coefficient h_2 as a function of the duty cycle d_c of the Hankel-phased rectangular grating. After (Sun et al., 2007)

6. References

Barlow, G. F.; Shore, A.; Turnbull, G. A. & Samuel, I. D. W. (2004). Design and analysis of a low-threshold polymer circular-grating distributed-feedback laser. *J. Opt. Soc. Am. B*, Vol. 21, No. 12, pp. 2142-2150

Brauch, U.; Loosen, P. & Opower, H. (2000). High-Power Diode Lasers for Direct Applications, In: *High-Power Diode Lasers: Fundamentals, Technology, Applications*. Diehl, R., (Ed.), pp. 303-368, Springer, Berlin/Heidelberg

Chen, Y.; Li, Z.; Zhang, Z.; Psaltis, D. & Scherer, A. (2007). Nanoimprinted circular grating distributed feedback dye laser. *Appl. Phys. Lett.*, Vol. 91, No. 5, pp. 051109

Coccioli, R.; Boroditsky, M.; Kim, K. W.; Rahmat-Samii, Y. & Yablonovitch, E. (1998). Smallest possible electromagnetic mode volume in a dielectric cavity. *IEE Proc.-Optoelectron.*, Vol. 145, No. 6, pp. 391-397

Erdogan, T. & Hall, D. G. (1990). Circularly symmetric distributed feedback semiconductor laser: an analysis. *J. Appl. Phys.*, Vol. 68, No. 4, pp. 1435-1444

Erdogan, T. & Hall, D. G. (1992). Circularly symmetric distributed feedback laser: coupled mode treatment of TE vector fields. *IEEE J. Quantum Electron.*, Vol. 28, No. 3, pp. 612-623

Fallahi, M.; Dion, M.; Chatenoud, F.; Templeton, I. M.; Barber, R. & Sedivy, J. (1994). Low threshold CW operation of circular-grating surface-emitting DBR lasers using MQW and a self-aligned process. *IEEE Photon. Technol. Lett.*, Vol. 6, No. 11, pp. 1280-1282

Greene, P. L. & Hall, D. G. (2001). Effects of radiation on circular-grating DFB lasers—part II: device and pump-beam parameters. *IEEE J. Quantum Electron.*, Vol. 37, No. 3, pp. 364-371

Haus, H. A. (1975). Gain saturation in distributed feedback lasers. *Appl. Opt.*, Vol. 14, No. 11, pp. 2650-2652

Hecht, E. (1998). *Optics*, 3rd edn., Addison-Wesley

Iga, K. (2000). Surface-emitting laser—its birth and generation of new optoelectronics field. *IEEE J. Sel. Top. Quantum Electron.*, Vol. 6, No. 6, pp. 1201-1215

Jebali, A.; Mahrt, R. F.; Moll, N.; Erni, D.; Bauer, C.; Bona, G.-L. & Bachtold, W. (2004). Lasing in organic circular grating structures. *J. Appl. Phys.*, Vol. 96, No. 6, pp. 3043-3049

Jebali, A.; Erni, D.; Gulde, S.; Mahrt, R. F. & Bachtold, W. (2007). Analytical calculation of the *Q* factor for circular-grating microcavities. *J. Opt. Soc. Am. B*, Vol. 24, No. 4, pp. 906-915

Jordan, R. H.; Hall, D. G.; King, O.; Wicks, G. & Rishton, S. (1997). Lasing behavior of circular grating surface-emitting semiconductor lasers. *J. Opt. Soc. Am. B*, Vol. 14, No. 2, pp. 449-453

Kasunic, K. J.; Wright, E. M. & Peyghambarian, N. (1995). Numerical modeling of inhomogeneously-pumped circular-grating DFB lasers. *Proc. SPIE*, Vol. 2398, No. 1, pp. 125-134

Olson, C.; Greene, P. L.; Wicks, G. W.; Hall, D. G. & Rishton, S. (1998). High-order azimuthal spatial modes of concentric-circle-grating surface-emitting semiconductor lasers. *Appl. Phys. Lett.*, Vol. 72, No. 11, pp. 1284-1286

Scheuer, J. & Yariv, A. (2003). Coupled-waves approach to the design and analysis of Bragg and photonic crystal annular resonators. *IEEE J. Quantum Electron.*, Vol. 39, No. 12, pp. 1555-1562

Scheuer, J.; Green, W. M. J.; DeRose, G. A. & Yariv, A. (2005a). InGaAsP annular Bragg lasers: theory, applications, and modal properties. *IEEE J. Sel. Top. Quantum Electron.*, Vol. 11, No. 2, pp. 476-484

Scheuer, J.; Green, W. M.; DeRose, G. & Yariv, A. (2005b). Ultra-sensitive biochemical sensor based on circular Bragg micro-cavities, *Proceedings of Conference on Lasers and Electro-Optics/Quantum Electronics and Laser Science and Photonic Applications Systems Technologies*, pp. CPDA7, Baltimore, MD, May 2005, Optical Society of America

Scheuer, J. (2007). Direct rotation-induced intensity modulation in circular Bragg micro-lasers. *Opt. Express*, Vol. 15, No. 23, pp. 15053-15059

Shams-Zadeh-Amiri, A. M.; Li, X. & Huang, W. P. (2000). Above-threshold analysis of second-order circular-grating DFB lasers. *IEEE J. Quantum Electron.*, Vol. 36, No. 3, pp. 259-267

Shams-Zadeh-Amiri, A. M.; Li, X. & Huang, W. P. (2003). Hankel transform-domain analysis of scattered fields in multilayer planar waveguides and lasers with circular gratings. *IEEE J. Quantum Electron.*, Vol. 39, No. 9, pp. 1086-1098

Sun, X. K. & Yariv, A. (2007). Modal properties and modal control in vertically emitting annular Bragg lasers. *Opt. Express*, Vol. 15, No. 25, pp. 17323-17333

Sun, X. K.; Scheuer, J. & Yariv, A. (2007). Optimal design and reduced threshold in vertically emitting circular Bragg disk resonator lasers. *IEEE J. Sel. Top. Quantum Electron.*, Vol. 13, No. 2, pp. 359-366

Sun, X. K.; Scheuer, J. & Yariv, A. (2008). Optimal design of vertically emitting circular Bragg disk resonator lasers, *Proceedings of SPIE*, pp. 689604, SPIE Photonics West 2008, San Jose, CA, Jan. 2008, SPIE

Sun, X. K. & Yariv, A. (2008). Surface-emitting circular DFB, disk-, and ring- Bragg resonator lasers with chirped gratings: a unified theory and comparative study. *Opt. Express*, Vol. 16, No. 12, pp. 9155-9164

Sun, X. K. & Yariv, A. (2009a). Surface-emitting circular DFB, disk-, and ring- Bragg resonator lasers with chirped gratings. II: nonuniform pumping and far-field patterns. *Opt. Express*, Vol. 17, No. 1, pp. 1-6

Sun, X. K. & Yariv, A. (2009b). Surface-emitting circular DFB, disk-, and ring- Bragg resonator lasers with chirped gratings. III: gain saturation effects and above-threshold analysis. *Opt. Express*, Vol. 17, No. 12, pp. 10119-10125

Sun, X. K. & Yariv, A. (2009c). A unified theory for surface emitting chirped circular grating lasers, *Proceedings of SPIE*, pp. 72180H, SPIE Photonics West 2009, San Jose, CA, Jan. 2009, SPIE

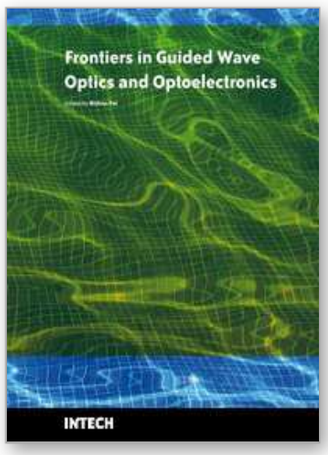
Turnbull, G. A.; Carleton, A.; Tahraouhi, A.; Krauss, T. F.; Samuel, I. D. W.; Barlow, G. F. & Shore, K. A. (2005). Effect of gain localization in circular-grating distributed feedback lasers. *Appl. Phys. Lett.*, Vol. 87, No. 20, pp. 201101

Wu, C.; Svilans, M.; Fallahi, M.; Makino, T.; Glinski, J.; Maritan, C. & Blaauw, C. (1991). Optical pumped surface-emitting DFB GaInAsP/InP lasers with circular grating. *Electron. Lett.*, Vol. 27, No. 20, pp. 1819-1821

Wu, C.; Svilans, M.; Fallahi, M.; Templeton, I.; Makino, T.; Glinski, J.; Maciejko, R.; Najafi, S. I.; Maritan, C.; Blaauw, C. & Knight, G. (1992). Room temperature operation of electrically pumped surface-emitting circular grating DBR laser. *Electron. Lett.*, Vol. 28, No. 11, pp. 1037-1039

Wu, C.; Makino, T.; Fallahi, M.; Craig, R. G. A.; Knight, G.; Templeton, I. & Blaauw, C. (1994). Novel circular grating surface-emitting lasers with emission from center. *Jpn. J. Appl. Phys.*, Vol. 33-Pt. 2, No. 3B, pp. L427-L429

Yariv, A. (1989). *Quantum Electronics*, 3rd edn., Wiley, New York



Frontiers in Guided Wave Optics and Optoelectronics
Edited by Bishnu Pal

ISBN 978-953-7619-82-4
Hard cover, 674 pages
Publisher InTech
Published online 01, February, 2010
Published in print edition February, 2010

As the editor, I feel extremely happy to present to the readers such a rich collection of chapters authored/co-authored by a large number of experts from around the world covering the broad field of guided wave optics and optoelectronics. Most of the chapters are state-of-the-art on respective topics or areas that are emerging. Several authors narrated technological challenges in a lucid manner, which was possible because of individual expertise of the authors in their own subject specialties. I have no doubt that this book will be useful to graduate students, teachers, researchers, and practicing engineers and technologists and that they would love to have it on their book shelves for ready reference at any time.

How to reference
In order to correctly reference this scholarly work, feel free to copy and paste the following:

Xiankai Sun and Amnon Yariv (2010). Surface-Emitting Circular Bragg Lasers – A Promising Next-Generation On-Chip Light Source for Optical Communications, Frontiers in Guided Wave Optics and Optoelectronics, Bishnu Pal (Ed.), ISBN: 978-953-7619-82-4, InTech, Available from: http://www.intechopen.com/books/frontiers-in-guided-wave-optics-and-optoelectronics/surface-emitting-circular-bragg-lasers-a-promising-next-generation-on-chip-light-source-for-optical-

INTECH
open science | open minds

InTech Europe
University Campus STeP Ri
Slavka Krautzeka 83/A
51000 Rijeka, Croatia
Phone: +385 (51) 770 447
Fax: +385 (51) 686 166
www.intechopen.com

InTech China
Unit 405, Office Block, Hotel Equatorial Shanghai
No.65, Yan An Road (West), Shanghai, 200040, China
中国上海市延安西路65号上海国际贵都大饭店办公楼405单元
Phone: +86-21-62489820
Fax: +86-21-62489821

© 2010 The Author(s). Licensee IntechOpen. This chapter is distributed under the terms of the Creative Commons Attribution-NonCommercial-ShareAlike-3.0 License, which permits use, distribution and reproduction for non-commercial purposes, provided the original is properly cited and derivative works building on this content are distributed under the same license.

IntechOpen

IntechOpen